

Self-Assembly of Aromatic Amino Acid Enantiomers into Supramolecular Materials of High Rigidity

Santu Bera, Bin Xue, Pavel Rehak, Guy Jacoby, Wei Ji, Linda J. W. Shimon, Roy Beck, Petr Král, Yi Cao, and Ehud Gazit*

Cite This: *ACS Nano* 2020, 14, 1694–1706

Read Online

ACCESS |

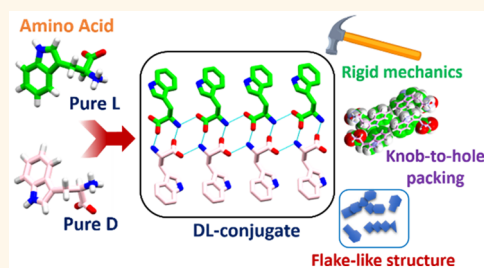
Metrics & More

Article Recommendations

Supporting Information

ABSTRACT: Most natural biomolecules may exist in either of two enantiomeric forms. Although in nature, amino acid biopolymers are characterized by L-type homochirality, incorporation of D-amino acids in the design of self-assembling peptide motifs has been shown to significantly alter enzyme stability, conformation, self-assembly behavior, cytotoxicity, and even therapeutic activity. However, while functional metabolite assemblies are ubiquitous throughout nature and play numerous important roles including physiological, structural, or catalytic functions, the effect of chirality on the self-assembly nature and function of single amino acids is not yet explored. Herein, we investigated the self-assembly mechanism of amyloid-like structure formation by two aromatic amino acids, phenylalanine (Phe) and tryptophan (Trp), both previously found as extremely important for the nucleation and self-assembly of aggregation-prone peptide regions into functional structures. Employing D-enantiomers, we demonstrate the critical role that amino acid chirality plays in their self-assembly process. The kinetics and morphology of pure enantiomers is completely altered upon their coassembly, allowing to fabricate different nanostructures that are mechanically more robust. Using diverse experimental techniques, we reveal the different molecular arrangement and self-assembly mechanism of the DL-racemic mixtures that resulted in the formation of advanced supramolecular materials. This study provides a simple yet sophisticated engineering model for the fabrication of attractive materials with bionanotechnological applications.

KEYWORDS: functional metabolite, amino acids, chirality, self-assembly, nanomaterials, bionanotechnology



Metabolites are the simplest building blocks utilized by biological systems, performing a multitude of functions.¹ The propensity of metabolites to self-assemble into distinct nanostructures displaying diverse material properties is abundant in nature.² Inspired by nature, mimicking the naturally occurring processes of metabolites' self-assembly into distinct structure is now considered to be a promising approach to achieve revolutionary advances in the design and fabrication of attractive functional materials.^{1,3} Similar to protein amyloids, self-assembly of amyloid fiber forming single amino acids has been explored to design exciting biomaterials.^{4–6} Aromatic amino acids such as Phe, Trp, Tyr, and His are reported to form a wide range of nanostructures including fibers, nanotubes, nanoribbons, twisted nanosheets, dendritic structures, *etc.*, depending on the self-assembly conditions.^{5,6} Apart from morphological diversity, a recent report showed the efficiently dense packing of β -Gly crystals along certain crystallographic planes provided a high piezoelectric voltage constant, higher than the voltage produced by any currently used ceramic and polymeric

materials.⁷ Nonpolar centrosymmetric crystals of α -Gly have been demonstrated to exhibit surface pyroelectricity.^{8,9} Recently, our group has revealed the intrinsic fluorescence properties of amyloid-like structures fabricated by single amino acids.¹⁰ The formation, dynamics, and cellular distribution of supramolecular chromophores were detected without the use of an external dye. However, due to their simplicity, the use of unimolecular amino acid assemblies to design attractive material has been limited by the lack of chemical diversity and functional complexity.

Chirality is a natural attribute of most biomolecules and bears universal significance for chemistry, physics, biology, and medicine.^{11–13} In an interesting strategy, it has been

Received: September 16, 2019

Accepted: January 16, 2020

Published: January 16, 2020

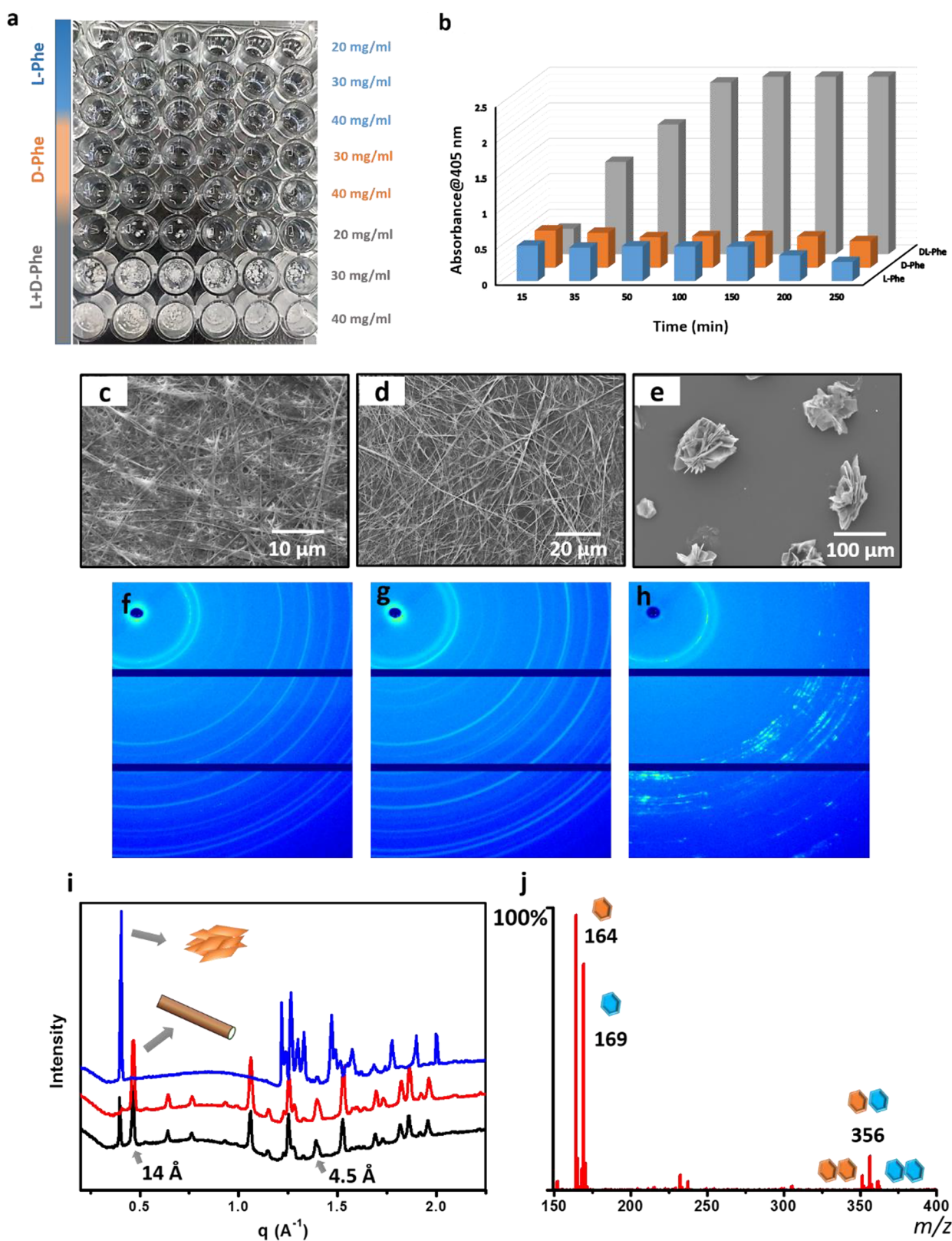


Figure 1. Self-assembly of pure and mixed Phe enantiomers. (a) Macroscopic visualization of the phase behavior after 24 h. (b) Kinetics of the 405 nm absorbance of the three systems (-L-, -D and -DL) at 30 mg/mL over a period of 4 h. (c–e) HR-SEM images of (c) L-Phe, (d) D-Phe, and (e) DL-Phe. (f–h) X-ray scattering 2D patterns of (f) L-Phe, (g) D-Phe, indicating random orientation of structures in the plane of the film, and (h) DL-Phe, indicating the presence of polycrystalline assemblies. (i) Corresponding azimuthally integrated spectra of L-Phe, D-Phe, and DL-Phe shown in black, red, and blue, respectively. (j) Mass spectra of the noncovalent assemblies of the intermolecular complexes. Hexagons represent D-Phe (yellow) and L-Phe (blue).

demonstrated that the concurrent presence of both amino acid enantiomers may significantly alter the functional properties of the resultant racemic mixture, compared to the pure enantiomers. The nonpolar L-Asp crystal was converted into a conglomerate of mixed polar sectors by incorporating different amounts of D-Asp.¹⁴ A pyroelectric effect was observed for the nonpolar crystals of L-Ala upon doping with the opposite enantiomer.^{14–16} Racemic amino acid crystals have also been reported to generate a voltage up to 2 times higher than amino acid crystals composed of a single isomer.¹⁷ Thus, the fabrication of chirality-induced attractive materials^{18–20} and their pharmaceutical design^{21–23} is an advanced avenue of research, resulting in more favorable packing and tunable properties. Several research groups have studied the effect of chirality on the self-assembly nature of short peptides, which can mimic that of large proteins.^{24–33} For example, Marchesan *et al.* have recently demonstrated that for tripeptides, only when the chirality of the N-terminal amino acid was different from that of the other amino acids were the resulting tripeptides able to form well-defined self-assembled structures, while no ordered structures was observed for the corresponding homochiral tripeptides.²⁸ Multicomponent gelators comprising amino acids of different chirality were reported to show completely altered behavior along with significantly different rheological properties that could not be achieved using their individual components.^{34–38} The mixed-enantiomers-based supramolecular gel showed enhanced mechanical and thermal strength.³⁹ The use of racemic peptides was also reported to increase the material rigidity of the well-known peptide gelator as compared to gels prepared from either pure enantiomer.⁴⁰ Also the use of a racemic mixture is known, for instance to favor peptide and protein crystallization.^{41,42} However, systematic demonstration of the effect of chirality on the self-assembly nature of single amino acids and the consequent modulation of the resulting functional characteristics has rarely been reported.⁴³

Due to the inherent properties of higher aggregation into ordered structures and their well-defined role in peptide self-assembly processes, aromatic amino acids L-Phe and L-Trp have been utilized for the design of interesting functionalities.^{44–46} Our group has previously presented the pioneering reports of the amyloid-like self-assembly properties of L-Phe and L-Trp.^{47,48} Subsequently, several other studies have reported the well-ordered nanostructure formation by L-Phe and L-Trp under different experimental conditions.^{5,6,43,49} Attempts to investigate the fiber-forming mechanism of L-Phe have shed some light regarding the participation of the $-\text{NH}_3^+$ and $-\text{COO}^-$ groups in hydrogen bonding and polar interactions.^{49–51} However, the detailed mechanism of the concentration-dependent stepwise self-assembly and structure formation by L-Trp in solution has not been fully described yet. Moreover, exploring the effect of D-enantiomers on the self-assembly pattern and the molecular arrangement of the resultant structural organization of aromatic single amino acids could demonstrate an exciting approach for the development of potentially applicative materials. Recently, we have deciphered the coassembly rule for amino acids based on the matching of their interlayer separation in single-crystal structures.^{52,53} In this context, the similar packing of two enantiomers of a particular amino acid could be expected to allow their coassembly to fabricate different materials with distinct properties from their parent pure enantiomers.

Herein, we investigated the self-assembly kinetics and the mechanism of structure formation by pure Phe and Trp enantiomers. Next, we explored the role of chirality in the self-assembly and function of the amino acids and the effect of chirality on the recognition of amino acids. The presence of the opposite chirality (racemate) was found to significantly alter the assembly kinetics and the resultant nanostructure morphologies and allowed the chirality-induced fabrication of different nanoarchitectures. Applying different experimental techniques, such as wide-angle X-ray scattering (WAXS) and molecular dynamics (MD) simulations, we demonstrated the differences in the mechanism of self-assembly and the structural organization of the single and mixed systems. Moreover, using atomic force microscopy (AFM) nano-indentation, we showed that the nanostructures produced by the Phe DL-composite possessed a much higher Young's modulus of 53.5 ± 12.1 GPa, compared to 5.8 ± 0.7 and 1.8 ± 0.3 GPa for the L- and D-isomer, respectively. Thus, these smart materials fabricated by the DL-racemic mixture could act as attractive candidates for future nanotechnological applications.

RESULTS AND DISCUSSION

Self-Assembly of Phe. To analyze the self-assembly of Phe, we first probed the phase behavior of the pure enantiomers (L and D) and their equimolar mixture at a wide range of concentrations up to 40 mg/mL. Dissolving either of the single enantiomers in double-distilled water by heating at 90 °C produced a clear solution, which remained clear over time, while cooling to room temperature, even at the 40 mg/mL concentration (Figure 1a,b). However, the phase behavior of the mixed DL (1:1) system was completely different. Although upon heating, the equimolar mixture of up to 40 mg/mL of D and L isomers fully dissolved in water and produced a clear solution, the turbidity of the solution began to increase immediately after starting to cool (Figure 1b). Moreover, in very short time, large flake-like structures were found to precipitate out from the solution, indicating a faster rate of aggregation for the DL-system. Figure 1c–e shows high-resolution scanning electron microscope (HR-SEM) images of the self-assembled nanostructures formed by the pure enantiomers and their mixed systems. Both L- and D-Phe formed micrometer-long singular fiber structures similar to the previously reported amyloid-like assemblies (Figure 1c,d).⁴⁷ However, the DL-system showed inhibition of fiber formation and fabrication of different types of aggregates, namely, crystalline flake-like structural assemblies (Figures 1e and S1). The formation of different types of morphologies coincided with their optical appearances over time, as observed from their turbidity assay. The level of turbidity was low for the more compact nanofibrillar structures of pure L and D isomers, while increased turbidity was measured for the DL-system due to a higher degree of light scattering from the large flakes (Figure 1b).

To structurally characterize the self-assembled pure and mixed enantiomeric systems, X-ray scattering experiments were performed (Figure 1f–i).⁵⁴ For pure L- and D-Phe, the fibers dried onto the Kapton film were randomly oriented in the plane of the film, producing an isotropic 2D powder diffraction (Figure 1f,g). The corresponding spectrum showed peaks at 4.5 Å, consistent with the repeating equatorial distance of the Phe ring along head-to-tail chains as observed in the single-crystal structure (Figures 1i and S2), along with a strong peak observed near 14 Å corresponding to the interlayer lateral

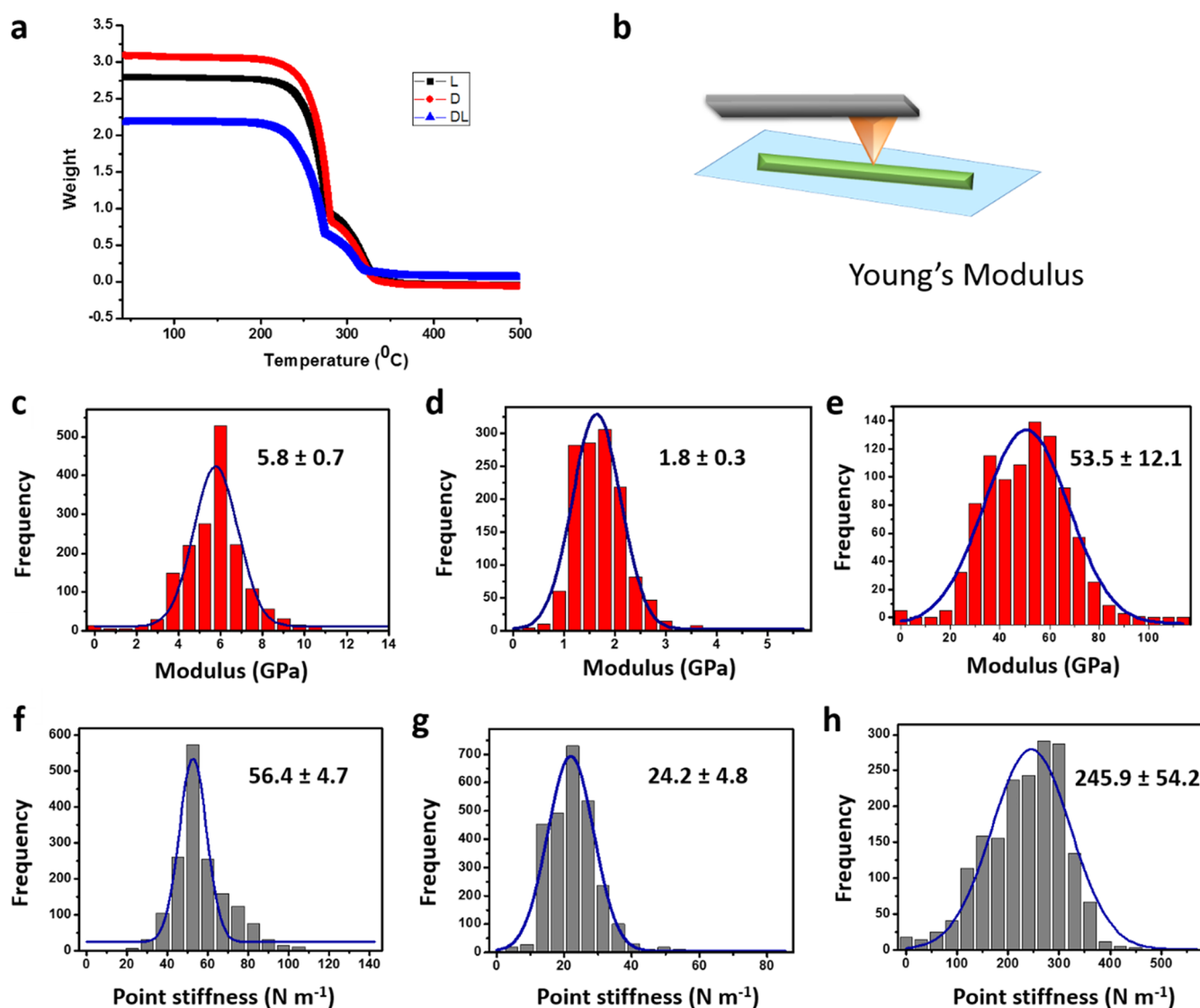


Figure 2. Thermal and mechanical properties of Phe self-assemblies. (a) TGA spectra of L-Phe and D-Phe fibers and DL-Phe crystalline flakes. (b) Schematic illustration of AFM nanoindentation employed to measure the mechanical properties of self-assembled nanostructures. (c–e) Young's modulus of (c) L-Phe, (d) D-Phe, and (e) DL-Phe. (f–h) Point stiffness calculated according to the linear relationship between Young's modulus and stiffness of (f) L-Phe, (g) D-Phe, and (h) DL-Phe.

separation distance in the thicker Phe fibers. In contrast, the 2D image of the DL system showed a completely different pattern, indicating the presence of polycrystalline assemblies. The anisotropic scattering image suggested the flakes were preferentially oriented in certain directions (Figure 1h). The presence of bright spots in particular places indicated significant deflection of scattering toward the specific directions. The corresponding spectrum showed a shift of both peaks corresponding to the equatorial and lateral distances toward a higher d -spacing value, signifying an altered arrangement of D- and L-Phe molecules in the mixture (Figure 1i). The crystal structure analysis of the pure enantiomers showed that Phe self-assembled *via* $-\text{NH}_3^+$ and $-\text{COO}^-$ groups of neighboring molecules interacting through hydrogen bonding and polar interactions (Figure S2).⁵⁵ The resulting two-dimensional H-bonded network structure imposed a very much restricted condition on the Phe molecules. To get rid of this strain, tyrosine (Tyr, ortho-hydroxyl Phe) molecules, previously shown to form assembled structures *via* H-bonds

mediated by the $-\text{OH}$ and COO^- groups, were examined.⁴⁹ Both pure enantiomers (-L and -D) and the mixed DL-Tyr were found to assemble into a similar broom-type morphology due to straight H-bonds between $-\text{OH}$ and COO^- groups (Figure S3). The different assembly of Phe thus suggests an altered arrangement in DL-Phe that might provide a more strain-free environment to the molecules.

Recent advances in the field of mass spectrometry allow a detailed determination of the noncovalent interactions of small molecules with ordered biomolecular structures and meta-clusters.^{53,56,57} To get further confirmation of the presence of both D and L isomers in the flake-like structures, we used electron-spray-ionization mass spectrometry by mixing a deuterium level L-Phe(d_5) with D-Phe (1:1) (Figure 1j). For the mixed system, in addition to m/z peaks at 164 and 169 corresponding to pure D-Phe and L-Phe(d_5), a strong signal was observed at 356 emanating from their composite materials. This analysis clearly established the formation of an enantiomeric conjugate in the mixed system, accounting for

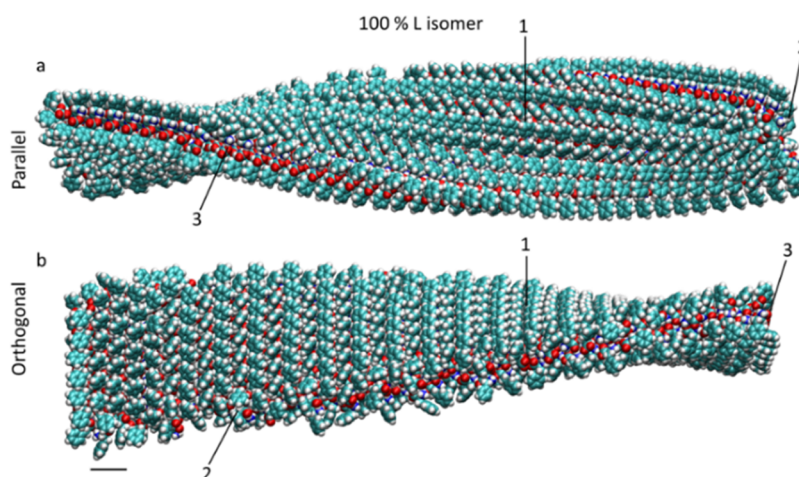


Figure 3. MD simulations of pure L-Phe crystals. (a) Pure L-Phe crystal cut along an aromatic zipper after 20 ns of simulation. (b) Pure L-Phe crystal cut orthogonally to the aromatic zipper after 20 ns of simulations. (1) Top bilayer facet, (2) the facet parallel to the aromatic zipper, and (3) the facet orthogonal to the aromatic zipper. Scale bar represents 1 nm.

the altered properties compared to the pure enantiomers. The coassembly formation was further confirmed by circular dichroism (CD) spectroscopy (Figure S4). L-Phe showed a positive peak around 220 nm, in line with the previously reported spectrum of Phe.⁵⁸ D-Phe gave rise to a mirror image spectrum, with a strong peak in the same wavelength but displaying a negative Cotton effect, as expected. The CD signal of the DL mixture was almost flat close to the baseline, indicating coassembly and the formation of an aggregate containing both enantiomers.

To check whether the coassembly formation and subsequent fabrication of different composite materials induced interesting properties, we investigated the thermal and mechanical stability of the studied amino acid systems. In the macroscale, thermal gravimetric analysis (TGA) characterization demonstrated both pure and mixed systems to be stable up to 250 °C, indicating their similar thermal stability (Figure 2a). To describe the mechanical rigidity of the crystals, Young's modulus and point stiffness were calculated. We used nanoindentation through AFM to measure the micromechanical properties of the pure and composite materials (Figure 2b–h).^{59,60} Typically, the cantilever approached the surface of the crystals and retracted at a constant speed, and the Young's modulus was obtained by fitting the force–distance traces with the Hertz model (Figure 2b). The measured elasticity of the L-Phe fibers showed a Young's modulus of 5.8 ± 0.7 GPa along the elongated direction, indicating a lower mechanical stability compared to the Phe–Phe dimer,⁶¹ and a point stiffness value of 56.4 ± 4.7 N m⁻¹ (Figure 2c,f). The D-enantiomer showed a Young's modulus and point stiffness of 1.8 ± 0.3 GPa and 24.2 ± 4.8 N m⁻¹, respectively (Figure 2d,g). However, the DL-composite materials displayed a highly increased Young's modulus of 53.5 ± 12.1 GPa, with a point stiffness of 245.9 ± 54.2 N m⁻¹ (Figure 2e,h). The observed Young's modulus value is particularly high for bioorganic materials, as other biomaterials like naturally derived DNA-based structures (0.3–2 GPa)^{62,63} and insulin self-assembling nanofibers (0.28 GPa)⁶⁴ show a significantly lower value. These data indicated a strong molecular packing in the DL-mixed system compared to the pure enantiomers, resulting in the formation of rigid materials displaying sufficiently high mechanostability to be useful for biomaterial applications.

We used atomistic molecular dynamics (MD) simulations to model Phe crystals. Since the structure of the racemic Phe crystal is not known, we simulated only one pure enantiomer, L-Phe crystal. First, we prepared small bilayer Phe crystals, with structures shown in Figure 3. These elongated crystals were cut either along the well-visible aromatic zipper or orthogonal to it, producing two crystals of $40 \times 8 \times 2$ or $8 \times 40 \times 2$ amino acids, placed in physiological solutions under ambient conditions (see Materials and Methods). Figure 3a,b reveal that after 20 ns of simulations, these L-Phe crystals had a tendency to fold in both parallel and orthogonal directions relative to the aromatic zipper. This tendency toward folding might promote the crystal to grow in a linear fashion, most likely along the zipper.

These simulations reveal that the chirality of amino acids and the lack of central symmetry in the crystals formed by these molecules promote crystal bending. Moreover, crystals formed by enantiomers of the same amino acid should be mirror images of each other. Therefore, their simple combination would give rise to flat racemic crystals. Real racemic crystals would contain the same number of both enantiomers suitably packed in their elementary cells, thus producing flat crystals.

Next, we simulated the dynamics of L-Phe on the surfaces of the crystals and calculated the binding energies of amino acids nested on the crystal facets (see Supporting Information). The results reveal that the top bilayer (facet 1 in Figure 3) is highly stable, due to hydrogen-bonding networks between zwitterion groups of the amino acids, which keep the bilayers intact. Additional bilayers bind to the top bilayer through weaker C–H–H–C dispersion interactions, which would slow down growth in this direction. The amino acids show a large mobility on the L-Phe crystal facets, which are parallel and orthogonal to the aromatic zipper (facets 2, 3, respectively, in Figure 3). The amino acids in the facet parallel to the aromatic zipper (facet 2 in Figure 3) show relatively strong binding with other amino acids in the same facet, but not with the remainder of the crystal. In the facet orthogonal to the aromatic zipper (facet 3 in Figure 3), the situation is opposite. These results show that growth on the facet parallel to the aromatic zipper is more likely to continue and produce twisted 1D crystals. The D-isomer is only a mirror image of the L-isomer. Thus, the

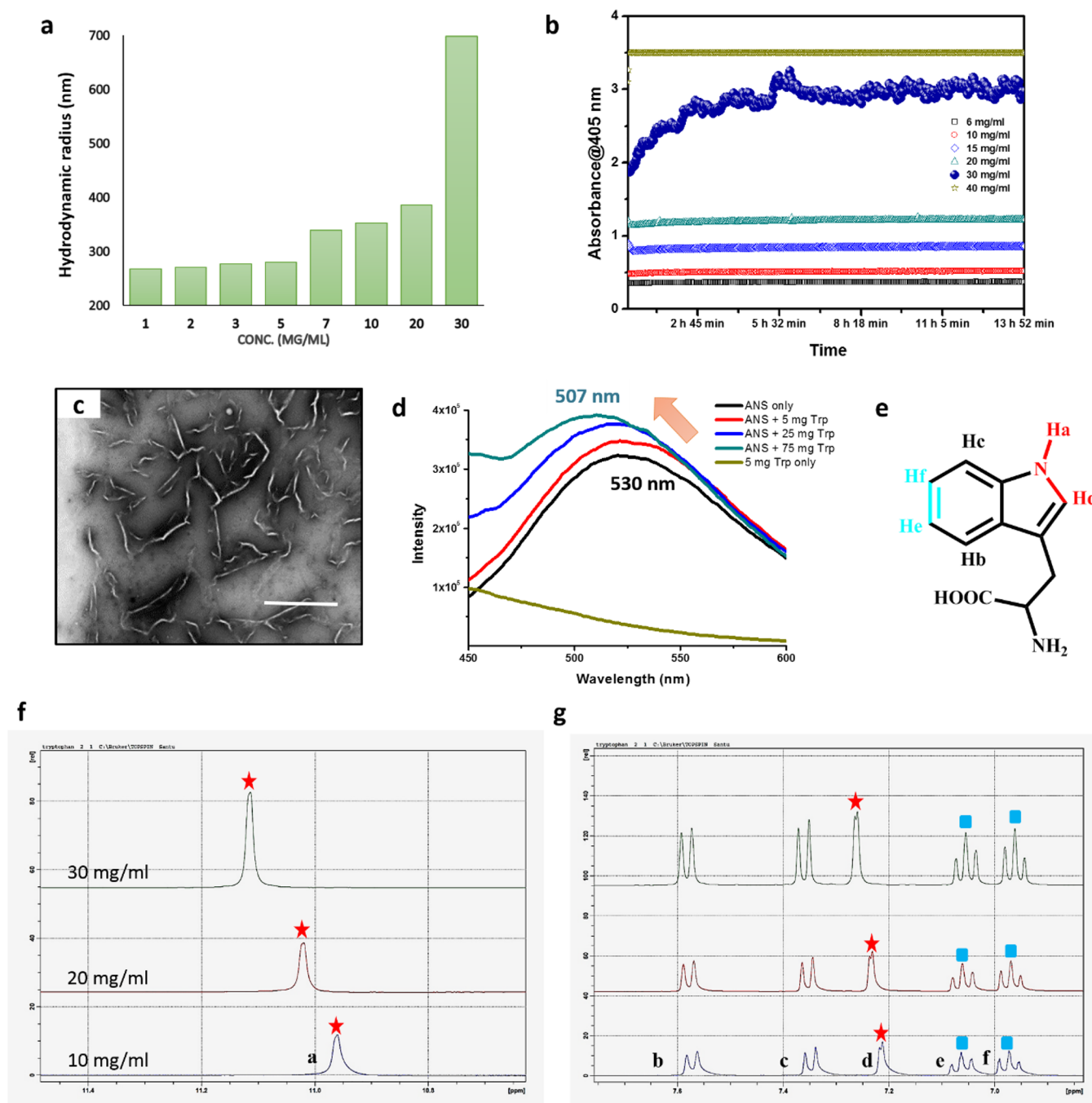


Figure 4. Self-assembly of *L*-Trp. (a) DLS assay with increasing concentration showing sudden increase in size of structures at 30 mg/mL concentration due to self-assembly. (b) Kinetics of phase behavior for different concentrations as observed by the absorbance at 405 nm over a period of 14 h. (c) TEM image of self-assembled nanostructures. (d) ANS binding fluorescence assay showing the change of surface environment from hydrophilic to hydrophobic. (e) Chemical structure of *L*-Trp with the different protons marked in different colors. (f, g) NMR spectrum showing the ^1H chemical shift (d, ppm) of (f) pyrrole $\text{N}-\text{H}_a$ and (g) aryl protons (H_d , H_e , H_f) at increasing concentrations. Scale bar of (c) is 2 μm .

evolutions of the *D*-isomer will be a mirror image of the *L*-isomer and will also grow into 1D twisted structures.

Self-Assembly of Trp. The chirality-induced structural modulation and consequent appearance of attractive mechanical properties of Phe inspired us to investigate the characteristics of another important aromatic amino acid, Trp. Initially, the self-assembly nature of pure *L*-Trp was studied by measuring the size of the resultant nanostructures at increasing concentrations using dynamic light scattering (DLS) (Figure

4a). The results showed that the size abruptly increased at a concentration of 30 mg/mL, indicating an extensive high aggregation. While at lower concentrations the solution remained clear, at 30 mg/mL the turbidity raised over time (Figures 4b and S5). The self-assembled morphology was studied by transmission electron microscopy (TEM). Short fibers 50–100 nm in diameter and several micrometers in length were observed (Figures 4c and S6), similar to our earlier report.⁴⁸ Previous simulation annealing also showed that *L*-Trp

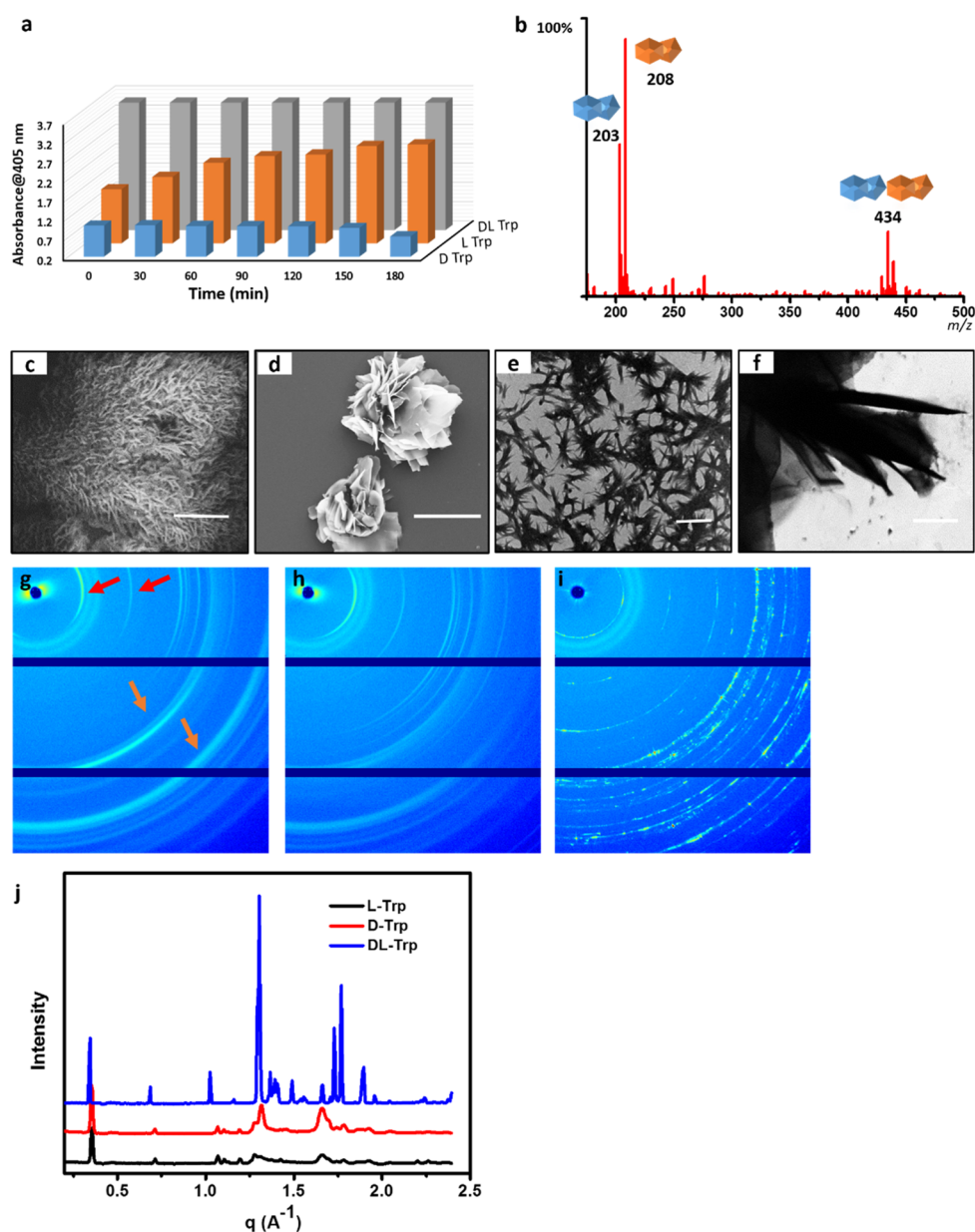


Figure 5. Modulation of L-Trp self-assembly by incorporation of D-Trp. (a) Kinetics of the 405 nm absorbance of the 30 mg/mL solutions over a time period of 3 h. (b) Mass spectra of the noncovalent assemblies of the intermolecular complexes. (c–f) HR-SEM and TEM images of (c and e) D-Trp and (d and f) DL-Trp. (g–i) X-ray scattering 2D patterns of (g) L-Trp, (h) D-Trp, and (i) DL-Trp. (j) Corresponding azimuthally integrated spectra. Scale bar for (c) and (d) is 50 μm and for (e) and (f) is 1 μm .

molecules stacked into a tubular structure with a 4-fold symmetry and folded into extremely well-organized fibrillar structures similar to those of Phe, where hydrophilic termini were positioned internally and the hydrophobic rings resided externally, exposed to the solvent.⁶⁵ To experimentally probe the role of the aromatic ring in the self-assembly process of L-Trp, an ANS (8-anilino-1-naphthalenesulfonic acid) binding assay was employed. ANS is a widely used fluorescent reagent that blue shifts with a higher quantum yield upon changing the surface environment from hydrophilic to hydrophobic as also observed for Phe.⁴³ With elevated concentrations of L-Trp, an increase in the fluorescence intensity of ANS with concomitant blue shift of the maxima from 530 nm to 507 nm was observed (Figure 4d). These dose-dependent changes of fluorescence maxima suggested a change of the environment toward higher hydrophobicity, probably due to aromatic interactions.^{66,67}

The involvement of the aromatic protons in the self-assembly process was further investigated through concentration-dependent ^1H NMR spectroscopy (Figure 4e–g). Increasing the concentration from 10 mg/mL to 30 mg/mL resulted in an upfield shift of the aryl proton, H_c , and H_b , indicating their screening due to π – π interactions between aromatic rings. However, the indole N–H proton (H_a) and the nearby proton (H_d) shifted toward a higher ppm value, which specified the involvement of the N– H_a proton in hydrogen bonding at higher concentrations and conferred a change of the electronic environment in the nearby region.^{68,69}

To understand the effect of chirality on the self-assembly of L-Trp, we employed the D-Trp and thoroughly studied the effect in the racemic mixture. The phase behavior of pure D-Trp revealed to some extent different kinetics than that of L-Trp, as it did not show a change in turbidity over time at the

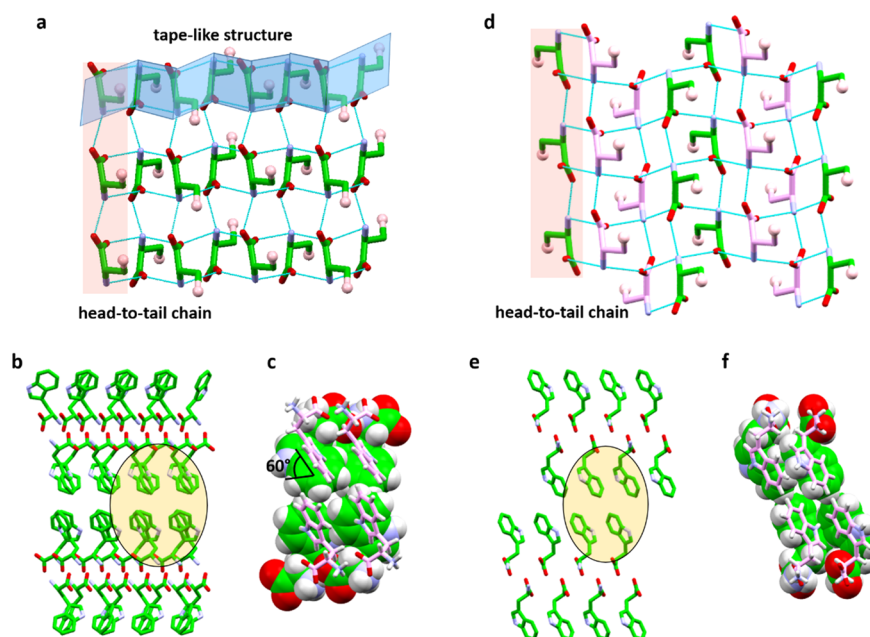


Figure 6. Single-crystal structural analysis of (a–c) L-Trp and (d–f) DL-Trp. L-Trp: (a) Molecular chain formation (pink) and tape-like arrangement (blue). (b) Supramolecular β -sheet structure. (c) Twisted angle between two adjacent aromatic rings highlighted by a yellow circle in (b). DL-Trp: (d) 3D network arrangement through H-bonding interactions of molecular chains (pink). (e) Supramolecular β -sheet structure. (f) “Knobs-in-holes” fitting of adjacent aromatic rings highlighted by a yellow circle in (e).

30 mg/mL concentrations, but formed structures in solution at higher concentration (Figures 5a and S5). ANS binding assay using D-Trp showed a similar change of environment from hydrophilic to hydrophobic, as also observed for L-Trp (Figure S7). The concentration-dependent NMR study also demonstrated a shift toward lower ppm values due to the screening of the aromatic proton as a result of π - π stacking (Figure S8). The characteristics of an equimolar mixture of D- and L-Trp (1:1) were completely different from those of their individual pure enantiomers. The turbidity of the DL-Trp solution increased very rapidly during cooling, even at the lower concentrations, indicating a higher aggregation rate for the enantiomeric mixed system (Figures 5a and S5), similar to DL-Phe. The formation of composite materials by the equimolar mixture of the L- and D-enantiomers was further confirmed by mass spectrometry. For the 1:1 mixture of D-Trp and L-Trp (*indole-d₅*), along with *m/z* peaks at 203 and 208 corresponding to their individual mass, a strong peak was observed at 434 due to the formation of the composite material (Figure 5b). CD spectra further confirmed the coassembly of the equimolar mixture of D- and L-Trp (Figure S9). The pure L- and D-Trp produced nearly mirror image peaks around \sim 223 nm. However, for the DL-mixed system, the spectrum was almost entirely flat and very close to the baseline, indicating the presence of racemic aggregates. The ANS binding (Figure S10) and NMR studies (Figure S11) of DL-Trp revealed the involvement of aromatic π - π interactions in the self-assembly process, as observed for pure D- and L-Trp. To investigate the underlying morphology, we employed HR-SEM and TEM analysis. Similar to L-Trp, D-Trp formed short fibers, several micrometers in length (Figure 5c,e). In contrast, as observed in both SEM and TEM images, the DL-conjugate fabricated completely different nanostructures, with a crystalline flake-like morphology (Figures 5d,f and S12).

The details of the molecular arrangement of the self-assembled nanostructures formed by pure and mixed

enantiomers were studied by WAXS, allowing the investigation of the supramolecular organization of the different systems at a local scale (Figure 5g–j). Pure L- or D-Trp produced powder diffraction 2D images with arc-centered intensity maxima, similar to pure Phe enantiomers (Figure 5g,h), reflecting the randomly oriented organization of the elongated structures. However, the presence of shorter fibers compared to Phe produced 2D scattering images that displayed a preferred orientation within the sample space, as each series of peaks was intensified along a specific angle (red and yellow arrows in Figure 5g). The spectrum containing all the peaks is shown in Figure 5j. The peak pertaining to the equatorial distance at 4.75 Å was consistent with the repeating unit distance between molecules observed in the single-crystal structure of pure L/D Trp.⁷⁰ The 17.5 Å peak was also consistent with the interlayer spacing, proposing lateral organization of Trp. However, the 2D image of the DL-conjugate showed a clear difference from the pure enantiomers. The scattering pattern suggested the formation of polycrystalline randomly oriented materials (Figure 5i). The corresponding spectrum also showed an altered position of the peaks of both equatorial and meridional distances along with the appearance of several additional peaks, further validating the formation of a different composite (Figure 5j). Moreover, alternation of the molecular packing was further supported by the inversion of the relative intensities of the meridional and equatorial peaks.

To gain further insight into the mechanism of molecular arrangement of the pure enantiomer and conjugate assemblies, single-crystal structures of L-Trp⁷⁰ and DL-Trp grown from water were analyzed in detail (Figure 6). The differences in their packing better clarified the difference in the resultant self-assembled nanostructures. L-Trp crystallized in space group P_1 with 16 molecules per asymmetric unit, in a pseudohexagonal arrangement. Along the crystallographic *b*-direction, the molecules were connected through head-to-tail H-bonding and fabricated a single molecular chain (marked in pink in

Figure 6a). Along the *a*-axis, the molecules were connected in a sideways fashion through two H-bonds on each side and thus produced a tape-like arrangement (marked in blue in Figure 6a). The H-bond distances for different previously reported Trp crystals are compared in Supplementary Table S5. In the higher order packing, L-Trp arranged in a layer-by-layer structure resembling a supramolecular β -sheet structure in which two adjacent layers were stabilized through aromatic interactions (Figure 6b).⁵² However, the aromatic surface of the stacking layers did not exactly fit in a “knobs-in-holes” manner, but rather oriented around a $\pm 60^\circ$ twisted angle and interacted through edge-to-face π - π stacking interactions (Figure 6c). For DL-Trp, a similar head-to-tail chain formation through H-bonding was observed (Figure 6d–f). Yet, the centrosymmetric dimer formation of two adjacent chains of DL-Trp could not take place in the structure of the single enantiomers, either L- or D-Trp. Moreover, the tape-like structural pattern of the pure enantiomer was missing in the arrangement of DL-Trp. In higher order packing, DL-Trp also arranged into a similar layer-by-layer organization (Figure 6e) but with perfect “knobs-in-holes” fitting of aromatic surfaces through face-to-face π - π interaction (Figure 6f). This additional stabilization of DL-Trp probably directed the self-assembly pattern of the racemic material toward a different conformation rather than the 1D fiber formed by the pure enantiomers.

These Trp systems were modeled like in Figure 3, including the racemic Trp crystal structure. The prepared small bilayer Trp crystals, with structures shown in Figure 6, consisted of either pure left-handed (L) isomers or from 50% left- and 50% right-handed (D) isomers. The crystals were again cut and simulated as before. Figure 7a,b reveal that after 20 ns the pure L-Trp crystal has a tendency to fold in a direction parallel to the aromatic zipper, but it undulates along the orthogonal

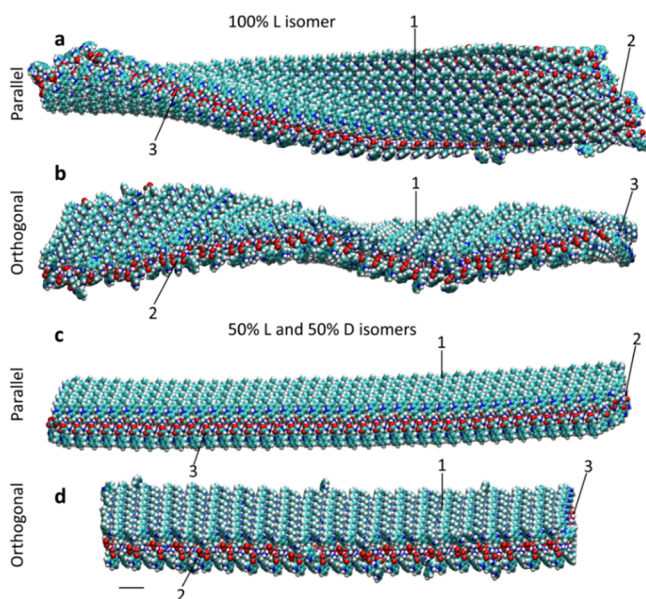


Figure 7. MD simulations of Trp crystals. L-Trp crystal cut (a) along an aromatic zipper and (b) orthogonally to the aromatic zipper after 20 ns. DL-Trp crystal cut (c) parallel to the aromatic zipper and (d) orthogonally to the aromatic zipper after 100 ns. Points showing (1) the top bilayer facet, (2) the facet parallel to aromatic zipper, and (3) the facet orthogonal to aromatic zipper. Scale bar represents 1 nm.

direction.⁴⁸ Thus, L(D)-Trp crystals might grow along the zipper (1D), in analogy to L(D)-Phe crystals. On the other hand, the mixed DL-Trp crystals stay on average flat, as shown in Figure 7c,d, since their possible twists are compensated by the presence of both enantiomers. The mixed DL-Trp crystals might grow in 2D or 3D.

L-Trp crystals have similar stability of facets like L-Phe crystals. In particular, the amino acids on the facet parallel to the aromatic zipper (facet 2 in Figure 7) show small mobility and relatively strong binding energies. In combination with the observed bending, it is likely that the crystal would grow in this 1D direction. In the DL-Trp crystal, the facet orthogonal to the aromatic zipper (facet 3 in Figure 7) is more stable, while the facet parallel to the zipper is less stable. This could be understood from the binding energies (Tables S3 and S4), showing that the same enantiomers have larger binding energies than opposite enantiomers (Supporting Information). However, a flat racemic crystal should be able to easily grow in both directions.

CONCLUSION

Aromatic amino acids play a crucial role in the formation of functional structures by the self-assembly of proteins and peptides, the major components of life. Our investigation of aromatic amino acid self-assembly together with the demonstration of the involvement of various interactions, such as electrostatic interactions, aromatic π - π stacking, hydrogen bonding, *etc.*, to drive the aggregation process provides the basis for understanding their self-assembly mechanism. Moreover, the experimental evidence presented here suggests different self-assembly kinetics and mechanisms for DL-composites of aromatic amino acids, allowing the fabrication of interesting materials with exciting physical properties compared to the pure enantiomers. Previously reported protein crystallography revealed that a racemic mixture of the enantiomeric forms of a protein molecule can crystallize in ways not obtainable by natural proteins.⁴¹ In addition, several experimental data support a theoretical prediction that racemic protein mixtures are highly amenable to crystallization due to the accessibility of several highly preferred achiral space groups. The high aggregation propensity of DL-amino acids to form self-assembled structures compared to the pure enantiomers, as observed in the current study, also supports a similar phenomenon for single amino acids. Moreover, the single-crystal structure analysis clearly demonstrated a favorable knob-to-hole packing of aromatic rings in the DL-mixture, which induced the easy growth of racemic crystals and the fabrication of self-assembled rigid materials. This study provides a different direction for chirality-induced tailor-made fabrication of futuristic functionalities based on natural systems for diverse nanotechnological applications.

MATERIALS AND METHODS

Materials. All amino acids were purchased from Sigma-Aldrich (purity >98%).

Turbidity Analysis. Turbidity analysis for the pure and composite amino acids was conducted by preparing fresh solutions at different concentrations in deionized water. Then, 200 μ L aliquots were pipetted into a 96-well plate, which was sealed using a Breathe-Easy sealing membrane (Sigma-Aldrich, Rehovot, Israel), and absorbance at 405 nm was measured over time. All measurements were performed using a Synergy HT plate reader (CLARIOstar, BAAG LABTECH) at 25 $^\circ$ C.

Scanning Electron Microscopy (SEM). The amino acids were dissolved in deionized water at a concentration of 2 mg/mL by heating to 90 °C followed by gradual cooling of the solutions. For DL-composites, 1 mg of each amino acids was similarly dissolved in 1 mL of deionized water. A 5 μ L aliquot was allowed to dry on a microscope glass coverslip at ambient conditions overnight and coated with Au. SEM images were recorded using a JSM-6700F FE-SEM (JEOL, Tokyo, Japan) operating at 10 kV.

Transmission Electron Microscopy. The amino acids were dissolved in deionized water at a concentration of 2 mg/mL by heating to 90 °C followed by gradual cooling of the solutions. For DL-composites, 1 mg of each amino acid was similarly dissolved in 1 mL of deionized water. A 10 μ L aliquot of the amino acid solution was placed on a 300-mesh copper grid. After 1 min, excess fluids were removed. For negative staining, the grid was stained with freshly prepared 2% uranyl acetate in water, and after 2 min, excess fluid was removed from the grid. Samples were viewed using a JEOL 1200EX electron microscope operating at 80 kV.

Mass Spectrometry. Samples were prepared for mass spectrometry by dissolving the amino acids in deionized water at a concentration of 1 mM by heating to 90 °C. Mass spectrometry was recorded using an Acquity UPLC system coupled to a TQD XEVO triple quadrupole ESI source mass spectrometer system from Waters (Milford, MA, USA).

Wide-Angle X-ray Scattering. The amino acids were dissolved in deionized water at a concentration of 2 mg/mL for individual amino acids or 1 mg/mL each for DL-composites by heating to 90 °C. The assembled structures were drop-cast over a thin Kapton film and left to dry in the presence of a magnetic field to produce aligned structures. WAXS measurements were performed using an in-house X-ray scattering system, with a GeniX (Xenocs) low-divergence Cu K α radiation source (wavelength of 1.54 Å) and a scatterless slits setup.⁷¹ Two-dimensional scattering data, with a momentum transfer wave vector (q) range of 0.07–2.5 Å⁻¹ at a sample-to-detector distance of approximately 160 mm, were collected on a Pilatus 300 K detector (Dectris, Baden-Daettwil, Switzerland) and radially integrated using Matlab (MathWorks, Natick, MA, USA)-based procedures (SAXSi). Calibration was performed using silver behenate. The scattering data of the empty Kapton film was collected as background and subtracted from the sample measurement.

Thermal Gravimetric Analysis. TGA experiments were performed using a TA Instruments (USA) module SDT 2950, at a temperature range between 40 and 510 °C with a heating rate of 10 °C min⁻¹, under a dry ultrahigh-purity argon atmosphere.

Fluorescence. For fluorescent emission characterization, the solution was incubated in a clean quartz cuvette, and the spectra were collected using a FluoroMax-4 spectrofluorometer (Horiba Jobin Yvon, Kyoto, Japan) at ambient temperature. The excitation wavelength was set at 350 nm with a slit of 5 nm and a step of 20 nm, and the emission wavelength was set at 400–660 nm with a slit of 5 nm and a step of 2 nm. Deionized water was used as background and subtracted.

Nuclear Magnetic Resonance. All NMR studies were carried out on a Bruker AVANCE 500 MHz spectrometer at 278 K. Amino acid concentrations were in the range of 10–30 mg/mL in DMSO- d_6 .

Young's Modulus Measurement. Experiments were carried out using a commercial AFM (JPK, Nanowizard II, Berlin, Germany). The force curves were obtained using the commercial software from JPK and analyzed by a custom-written procedure based on Igor pro 6.12 (Wavemetrics Inc.). Silica cantilevers (RTESPA-525 Bruker Company with the half-open angle of the pyramidal face of $\theta < 10^\circ$, tip radius ~ 8 nm, frequency in air ~ 525 kHz) were used in all experiments. The spring constant of the cantilevers was about 200 N m⁻¹. The maximum loading force was set to 1 μ N for the amino acid crystals. All AFM nanoindentation experiments were carried out at room temperature. In a typical experiment, the amino acid crystals were spread over the surface of a freshly cleaved mica substrate. Then, the cantilever was moved over the crystal with the help of an optical microscope at a constant speed of 2 μ m s⁻¹ and held on the crystal surface at a constant force of 1 μ N. Then, the cantilever was retracted

and moved to another spot for the next cycle. The indentation fit was performed using a custom-written Igor program and manually checked after the fitting. Each approaching force–deformation curve in the range of 30 nm, or from the contact point to the maximum indentation depth, if the maximum indentation depth was less than 30 nm, was fitted. By fitting the approaching curve to the Hertz model (1), the Young's modulus of the crystals was obtained. Typically, 4 or 5 such regions (3 μ m \times 3 μ m, 400 pixels) were randomly selected for each sample to construct the elasticity histogram.

$$F(h) = \frac{2}{\pi} \tan \alpha \frac{E}{1 - \nu^2} h^2 \quad (1)$$

where F is the force acting on the cantilever, h is the indentation depth of the crystal by the cantilever tip, α is the half-angle of the tip, E is the Young's modulus of the sample, and ν is the Poisson ratio. $\nu = 0.5$ was used in all calculations.

Point Stiffness Calculation. The measured point stiffness (k_{meas}) is composed of the stiffness constants of the cantilever (k_{can}) and the crystals (k_{cry}). Assuming that the crystal and the cantilever act as two serial springs, the point stiffness of the crystal can be calculated using eq 2. To estimate the material property of the crystals, we assumed that the mechanical behavior of the crystal could be described as linear elastic, which is a good approximation for solids under small strains.

$$k_{\text{cry}} = \frac{k_{\text{can}} k_{\text{meas}}}{k_{\text{can}} - k_{\text{meas}}} \quad (2)$$

Crystal Preparation and Data Collection. Crystals used for data collection were grown using the vapor diffusion method. The dry amino acid was first dissolved in D₂O, at a concentration of 5 mg/mL. Then, 50 μ L was deposited into a series of 8 \times 40 mm vessels. Each tube was sealed with Parafilm, in which a single small hole was pricked using a needle. The samples were placed inside a larger vessel filled with 2 mL of acetonitrile. The systems were ultimately capped and incubated at 18 °C for several days. Crystals typically grew within 7–8 days. For data collection, crystals were coated in Paratone oil (Hampton Research), mounted on a MiTeGen cryo-loop, and flash frozen in liquid nitrogen. Diffraction data were collected at 100 K on a Rigaku XtaLabPro with a Dectris Pilatus 3R 200 K A detector using Cu K α radiation at $\lambda = 1.54184$ Å.

Processing and Structural Refinement of Crystal Data. The diffraction data were processed using CrysAlisPro 1.171.39.22a. The structure was solved by direct methods using SHELXT-2014/5.⁷² The refinements were performed with SHELXL-2016/4 and weighted full-matrix least-squares against $|F^2|$ using all data. Atoms were refined independently and anisotropically, with the exception of hydrogen atoms, which were placed in calculated positions and refined in a riding mode. Crystal data collection and refinement parameters are shown in Supplementary Table 6, and the complete data can be found in the cif file as Supporting Information. The crystallographic data have been deposited in the CCDC with nos. 1522755 and 1943707 for D-Phe and DL-Trp, respectively.

MD Simulation. The MD simulations were performed with NAMD2.12 and NAMD 2.13 packages,⁷³ using a CHARMM 27 force field.⁷⁴ Atomistic MD simulations were performed under physiological conditions, *i.e.*, [NaCl] = 0.15 M, where the amino acids were in zwitterionic form. The TIP3P model was used for water molecules. The simulations were described by a Langevin dynamics in an NPT ensemble with $P = 1$ atm and $T = 310$ K. A Particle Mesh Ewald⁷⁵ summation was used to calculate long-range Coulombic interactions, with a grid spacing of 1.0. Short-range dispersion interactions used a switching algorithm, with an on/off distance of 10/12 Å. Pair lists were 13.5 Å, updated every 20 steps; 1–4 interactions were not scaled.

Crystal Bending Simulations. Left-handed and mixed enantiomer crystals were constructed using crystal structures.^{55,70} Each crystal has one bilayer held together by hydrogen bonding between 40 \times 8 \times 2 or 8 \times 40 \times 2 amino acids. Left-handed crystals were minimized for 50 000 steps and pre-equilibrated for 300 ps, with heavy amino acid

atoms constrained. Then, these crystals were released and simulated for 20 ns, with a time step of 2 fs and $\gamma_{\text{Lang}} = 1.00 \text{ ps}^{-1}$. Mixed enantiomer crystals were minimized for 20 000 steps and pre-equilibrated for 1–1.6 ns, with heavy amino acid atoms constrained. Then, the crystals were released and simulated for 100 ns.

Amino Acids Mobility Simulations. Here, the two types of crystals with dimensions of $12 \times 12 \times 12$ amino acids were in a physiological solution. First, the systems were minimized for 5000 steps, with heavy amino acid atoms constrained. Then, the systems were warmed for 2000 steps, with a time step of 1 fs, $\gamma_{\text{Lang}} = 1.00 \text{ ps}^{-1}$, and an increment of 1 K every 5 steps until the temperature reached 310 K. Then, the systems were pre-equilibrated with the same constraints for 1 ns and a time step of 1 fs. Afterward, the systems were further pre-equilibrated for 1 ns, a time step of 1 fs, and $\gamma_{\text{Lang}} = 0.01 \text{ ps}^{-1}$, while eliminating constraints on one side group of each amino acid of the central 10×10 amino acids on each facet. Finally, the central 10×10 amino acids were released, while all other heavy amino acid atoms were constrained and simulated for 30 ns at a time step of 2 fs.

Enthalpy of Binding Calculations. We calculated the enthalpy of amino acids binding to the crystal (described in the previous paragraph), using NAMD energy plugin version 1.4⁷³ in VMD.⁷⁶ Enthalpies of binding were calculated: (1) between amino acids and facets within which they were present and (2) between those amino acids and the remaining (constrained) amino acids in the crystal, ignoring solvent effects in both calculations. Enthalpy of binding was the sum of electrostatic and dispersion interactions, assuming Coulombic and 12–6 Lennard-Jones potentials, respectively. In the enthalpy calculations, the system parameters were kept the same as in the rest of the simulations. We calculated each enthalpy of binding every 10 ps for the entire 30 ns of simulation. We normalized the enthalpy terms with respect to the number of mobile amino acids (100 in each calculation) and averaged them over all snapshots.

ASSOCIATED CONTENT

Supporting Information

The Supporting Information is available free of charge at <https://pubs.acs.org/doi/10.1021/acsnano.9b07307>.

Single-crystal structure of L-Phe, HRSEM images of Phe and Tyr, CD spectra of Phe and Trp, macroscopic visualization of the phase behavior of Trp, TEM images of L-Trp and DL-Trp, ANS binding and NMR study of D-Trp and DL-Trp, supplementary note, Tables S1–S6 (PDF)

X-ray data (CIF)

X-ray data (CIF)

AUTHOR INFORMATION

Corresponding Author

Ehud Gazit – Tel Aviv University, Ramat Aviv, Israel;
orcid.org/0000-0001-5764-1720; Email: ehudg@post.tau.ac.il

Other Authors

Santu Bera – Tel Aviv University, Ramat Aviv, Israel;

orcid.org/0000-0002-4830-552X

Bin Xue – Nanjing University, Nanjing, People's Republic of China

Pavel Rehak – University of Illinois at Chicago, Chicago, Illinois

Guy Jacoby – Tel Aviv University, Tel Aviv, Israel

Wei Ji – Tel Aviv University, Ramat Aviv, Israel;

orcid.org/0000-0001-8982-5460

Linda J. W. Shimon – Weizmann Institute of Science, Rehovot, Israel; orcid.org/0000-0002-7861-9247

Roy Beck – Tel Aviv University, Tel Aviv, Israel

Petr Král – University of Illinois at Chicago, Chicago, Illinois; orcid.org/0000-0003-2992-9027

Yi Cao – Nanjing University, Nanjing, People's Republic of China; orcid.org/0000-0003-1493-7868

Complete contact information is available at:
<https://pubs.acs.org/doi/10.1021/acsnano.9b07307>

Notes

The authors declare no competing financial interest.

ACKNOWLEDGMENTS

This project received funding from the ERC under the European Union Horizon 2020 Research and Innovation Programme (grant agreement No BISON-694426 to E.G.). B.X. acknowledges support from the National Natural Science Foundation of China (Grant No. 11804148), the Natural Science Foundation of Jiangsu Province (No. BK20180320), and the Fundamental Research Funds for the Central Universities (No. 020414380118). R.B. acknowledges the support from the Israeli Science Foundation (550/15). The authors thank Dr. Sigal Rencus-Lazar for help in scientific and language editing.

REFERENCES

- (1) Aizen, R.; Tao, K.; Rencus-Lazar, S.; Gazit, E. Functional Metabolite Assemblies-A Review. *J. Nanopart. Res.* **2018**, *20*, 125.
- (2) Tadepalli, S.; Slocik, J.; Gupta, M.; Naik, R. R.; Singamaneni, S. Bio-Optics and Bio-Inspired Optical Materials. *Chem. Rev.* **2017**, *117*, 12705–12763.
- (3) Knowles, T. P. J.; Buehler, M. J. Nanomechanics of Functional and Pathological Amyloid Materials. *Nat. Nanotechnol.* **2011**, *6*, 469–479.
- (4) Ménard-Moyon, C.; Venkatesh, V.; Krishna, K. V.; Bonachera, F.; Verma, S.; Bianco, A. Self-Assembly of Tyrosine into Controlled Supramolecular Nanostructures. *Chem. - Eur. J.* **2015**, *21*, 11681–11686.
- (5) Babar, D. G.; Sarkar, S. Self-Assembled Nanotubes from Single Fluorescent Amino Acid. *Appl. Nanosci.* **2017**, *7*, 101–107.
- (6) Singh, P.; Brar, S. K.; Bajaj, M.; Narang, N.; Mithu, V. S.; Katara, O. P.; Wangoo, N.; Sharma, R. K. Self-Assembly of Aromatic α -Amino Acids into Amyloid Inspired Nano/Micro Scaled Architects. *Mater. Sci. Eng., C* **2017**, *72*, 590–600.
- (7) Guerin, S.; Stapleton, A.; Chovan, D.; Mouras, R.; Gleeson, M.; McKeown, C.; Noor, M. R.; Silien, C.; Rhen, F. M. F.; Kholkin, A. L.; Liu, N.; Soulimane, T.; Tofail, S. A. M.; Thompson, D. Control of Piezoelectricity in Amino Acids by Supramolecular Packing. *Nat. Mater.* **2018**, *17*, 180–186.
- (8) Piperno, S.; Mirzadeh, E.; Mishuk, E.; Ehre, D.; Cohen, S.; Eisenstein, M.; Lahav, M.; Lubomirsky, I. Water-Induced Pyroelectricity from Nonpolar Crystals of Amino Acids. *Angew. Chem., Int. Ed.* **2013**, *52*, 6513–6516.
- (9) Meirzadeh, E.; Sapir, L.; Cohen, H.; Cohen, S. R.; Ehre, D.; Harries, D.; Lahav, M.; Lubomirsky, I. Nonclassical Crystal Growth as Explanation for the Riddle of Polarity in Centrosymmetric Glycine Crystals. *J. Am. Chem. Soc.* **2016**, *138*, 14756–14763.
- (10) Shaham-Niv, S.; Arnon, Z. A.; Sade, D.; Lichtenstein, A.; Shirshin, E. A.; Kolusheva, S.; Gazit, E. Intrinsic Fluorescence of Metabolite Amyloids Allows Label-Free Monitoring of Their Formation and Dynamics in Live Cells. *Angew. Chem., Int. Ed.* **2018**, *57*, 12444–12447.
- (11) Jiang, S.; Chekini, M.; Qu, Z. B.; Wang, Y.; Yeltik, A.; Liu, Y.; Kotlyar, A.; Zhang, T.; Li, B.; Demir, H. V.; Kotov, N. A. Chiral Ceramic Nanoparticles and Peptide Catalysis. *J. Am. Chem. Soc.* **2017**, *139*, 13701–13712.

- (12) Yeom, J.; Yeom, B.; Chan, H.; Smith, K. W.; Dominguez-Medina, S.; Bahng, J. H.; Zhao, G.; Chang, W. S.; Chang, S. J.; Chuvilin, A.; Melnikau, D.; Rogach, A. L.; Zhang, P.; Link, S.; Král, P.; Kotov, N. A. Chiral Templating of Self-Assembling Nanostructures by Circularly Polarized Light. *Nat. Mater.* **2015**, *14*, 66–72.
- (13) Yang, G.; Zhang, S.; Hu, J.; Fujiki, M.; Zou, G. The Chirality Induction and Modulation of Polymers by Circularly Polarized Light. *Symmetry* **2019**, *11*, 474.
- (14) Mishuk, E.; Weissbuch, I.; Lahav, M.; Lubomirsky, I. Pyroelectricity in Nonpolar Directions in Crystals: Enantiomeric Disorder and Surface Wetting in Racemic α -Amino-Acids. *Cryst. Growth Des.* **2014**, *14*, 3839–3848.
- (15) Gomes, E. de M.; Viseu, T.; Belsley, M.; Almeida, B.; Costa, M. M. R.; Rodrigues, V. H.; Isakov, D. Piezoelectric and Pyroelectric Properties of DL-Alanine and L-Lysine Amino-Acid Polymer Nanofibers. *Mater. Res. Express* **2018**, *5*, No. 045049.
- (16) Meirzadeh, E.; Weissbuch, I.; Ehre, D.; Lahav, M.; Lubomirsky, I. Polar Imperfections in Amino Acid Crystals: Design, Structure, and Emerging Functionalities. *Acc. Chem. Res.* **2018**, *51*, 1238–1248.
- (17) Guerin, S.; O'Donnell, J.; Haq, E.; McKeown, C.; Silien, C.; Rhen, F. M. F.; Soulimane, T.; Tofail, S. A. M.; Thompson, D. Racemic Amino Acid Piezoelectric Transducer. *Phys. Rev. Lett.* **2019**, *122*, No. 047701.
- (18) Smith, D. K. Lost in Translation? Chirality Effects in the Self-Assembly of Nanostructured Gel-Phase Materials. *Chem. Soc. Rev.* **2009**, *38*, 684–694.
- (19) Moriuchi, T.; Hirao, T. Design of Ferrocene-Dipeptide Bioorganometallic Conjugates to Induce Chirality-Organized Structures. *Acc. Chem. Res.* **2010**, *43*, 1040–1051.
- (20) Liu, M.; Zhang, L.; Wang, T. Supramolecular Chirality in Self-Assembled Systems. *Chem. Rev.* **2015**, *115*, 7304–7397.
- (21) Sievers, S. A.; Karanicolas, J.; Chang, H. W.; Zhao, A.; Jiang, L.; Zirafi, O.; Stevens, J. T.; Münch, J.; Baker, D.; Eisenberg, D. Structure-Based Design of Non-Natural Amino-Acid Inhibitors of Amyloid Fibril Formation. *Nature* **2011**, *475*, 96–100.
- (22) Ridler, C. Alzheimer Disease: Misfolded Diabetes-Mellitus Peptide Seeds Amyloid-Beta Aggregation. *Nat. Rev. Neurol.* **2017**, *13*, 128.
- (23) Flemming, H.-C.; Wingender, J.; Szewzyk, U.; Steinberg, P.; Rice, S. A.; Kjelleberg, S. Biofilms: An Emergent Form of Bacterial Life. *Nat. Rev. Microbiol.* **2016**, *14*, 563–575.
- (24) Garcia, A. M.; Iglesias, D.; Parisi, E.; Styan, K. E.; Waddington, L. J.; Deganutti, C.; Zorzi, R. D.; Grassi, M.; Melchionna, M.; Vargiu, A. V.; Marchesan, S. Chirality Effects on Peptide Self-Assembly Unraveled from Molecules to Materials. *Chem.* **2018**, *4*, 1–15.
- (25) Wang, M.; Zhou, P.; Wang, J.; Zhao, Y.; Ma, H.; Lu, J. R.; Xu, H. Left or Right: How Does Amino Acid Chirality Affect the Handedness of Nanostructures Self-Assembled from Short Amphiphilic Peptides? *J. Am. Chem. Soc.* **2017**, *139*, 4185–4194.
- (26) Hu, K.; Jiang, Y.; Xiong, W.; Li, H.; Zhang, P. Y.; Yin, F.; Zhang, Q.; Geng, H.; Jiang, F.; Li, Z.; Wang, X.; Li, Z. Tuning Peptide Self-Assembly by an In-Tether Chiral Center. *Sci. Adv.* **2018**, *11*, No. eaar5907.
- (27) Luo, Z.; Wang, S.; Zhang, S. Fabrication of Self-Assembling D-Form Peptide Nanofiber Scaffold D-EAK16 for Rapid Hemostasis. *Biomaterials* **2011**, *32*, 2013–2020.
- (28) Marchesan, S.; Easton, C. D.; Styan, K.; Waddington, L.; Kushkaki, K.; Goodall, L.; Mclean, K.; Forsythe, J. S.; Hartley, P. G. Chirality Effects at each Amino Acid Position on Tripeptide Self-Assembly into Hydrogel Biomaterials. *Nanoscale* **2014**, *6*, 5172–5180.
- (29) Janek, K.; Rothmund, S.; Gast, K.; Beyermann, M.; Zipper, J.; Fabian, H.; Bienert, M.; Krause, E. Study of the Conformational Transition of $A\beta(1-42)$ Using D-Amino Acid Replacement Analogues. *Biochemistry* **2001**, *40*, 5457–5463.
- (30) Shi, J.; Du, X.; Yuan, D.; Zhou, J.; Zhou, N.; Huang, Y.; Xu, B. D-Amino Acid Modulate the Cellular Response of Enzymatic-Instructed Supramolecular Nanofibers of Small Peptides. *Biomacromolecules* **2014**, *15*, 3559–3568.
- (31) Zhao, Y.; Leman, L. J.; Search, D. J.; Garcia, R. A.; Gordon, D. A.; Maryanoff, B. E.; Ghadiri, M. R. Self-Assembling Cyclic D,L- α -Peptides as Modulators of Plasma HDL Function. A Supramolecular Approach toward Antiatherosclerotic Agents. *ACS Cent. Sci.* **2017**, *3*, 639–646.
- (32) Ye, Z.; Zhu, X.; Acosta, S.; Kumar, D.; Sang, T.; Aparicio, C. Self-Assembly Dynamics and Antimicrobial Activity of All L- and D-Amino Acid Enantiomers of a Designer Peptide. *Nanoscale* **2019**, *11*, 266–275.
- (33) Fu, Y.; Li, B.; Huang, Z.; Li, Y.; Yang, Y. Terminal is Important for the Helicity of the Self-Assemblies of Dipeptides Derived from Alanine. *Langmuir* **2013**, *29*, 6013–6017.
- (34) Marchesan, S.; Styan, K. E.; Easton, C. D.; Waddington, L.; Vargiu, A. V. Higher and Lower Supramolecular Orders for the Design of Self-Assembled Heterochiral Tripeptide Hydrogel Biomaterials. *J. Mater. Chem. B* **2015**, *3*, 8123–8132.
- (35) Marchesan, S.; Easton, C. D.; Kushkaki, F.; Waddington, L.; Hartley, P. G. Tripeptide Self-Assembled Hydrogels: Unexpected Twists of Chirality. *Chem. Commun.* **2012**, *48*, 2195–2197.
- (36) Pappas, C. G.; Frederix, P. W. J. M.; Mutasa, T.; Fleming, S.; Abul-Haija, Y. M.; Kelly, S. M.; Gachagan, A.; Kalafatovic, D.; Trevino, J.; Ulijn, R. V. Alignment of Nanostructured Tripeptide Gels by Directional Ultrasonication. *Chem. Commun.* **2015**, *51*, 8465–8468.
- (37) Basak, S.; Singh, I.; Ferranco, A.; Syed, J.; Kraatz, H.-B. On the Role of Chirality in Guiding the Self-Assembly of Peptides. *Angew. Chem., Int. Ed.* **2017**, *56*, 13288–13292.
- (38) McAulay, K.; Dietrich, B.; Su, H.; Scott, M. T.; Rogers, S.; Al-Hilaly, Y. K.; Cui, de H.; Serpell, L. C.; Seddon, A. M.; Draper, E. R.; Adams, D. J. Using Chirality to Influence Supramolecular Gelation. *Chem. Sci.* **2019**, *10*, 7801–7806.
- (39) Tómasson, D. A.; Ghosh, D.; Kržišnik, Z.; Fasolin, L. H.; Vicente, A. A.; Martin, A. D.; Thordarson, P.; Damodaran, K. K. Enhanced Mechanical and Thermal Strength in Mixed-Enantiomers-Based Supramolecular Gel. *Langmuir* **2018**, *34*, 12957–12967.
- (40) Nagy, K. J.; Giano, M. C.; Jin, A.; Pochan, D. J.; Schneider, J. P. Enhanced Mechanical Rigidity of Hydrogels Formed from Enantiomeric Peptide Assemblies. *J. Am. Chem. Soc.* **2011**, *133*, 14975–14977.
- (41) Yeates, T. O.; Kent, S. B. H. Racemic Protein Crystallography. *Annu. Rev. Biophys.* **2012**, *41*, 41–61.
- (42) Mandal, K.; Uppalapati, M.; Ault-Riché, D.; Kenney, J.; Lowitz, J.; Sidhu, S. S.; Kent, S. B. H. Chemical Synthesis and X-Ray Structure of a Heterochiral {D-Protein Antagonist Plus Vascular Endothelial Growth Factor} Protein Complex by Racemic Crystallography. *Proc. Natl. Acad. Sci. U. S. A.* **2012**, *109*, 14779–14784.
- (43) Singh, V.; Rai, R. K.; Arora, A.; Sinha, N.; Thakur, A. K. Therapeutic Implication of L-Phenylalanine Aggregation Mechanism and Its Modulation by D-Phenylalanine in Phenylketonuria. *Sci. Rep.* **2015**, *4*, 3875.
- (44) Reches, M.; Gazit, E. Casting Metal Nanowires within Discrete Self-Assembled Peptide Nanotubes. *Science* **2003**, *300*, 625–627.
- (45) Pawar, A. P.; DuBay, K. F.; Zurdo, J.; Chiti, F.; Vendruscolo, M.; Dobson, C. M. Prediction of “Aggregation-Prone” and “Aggregation-Susceptible” Regions in Proteins Associated with Neurodegenerative Diseases. *J. Mol. Biol.* **2005**, *350*, 379–392.
- (46) Frederix, P. W. J. M.; Scott, G. G.; Abul-Haija, Y. M.; Kalafatovic, D.; Pappas, C. G.; Javid, N.; Hunt, N. T.; Ulijn, R. V.; Tuttle, T. Exploring the Sequence Space for (Tri-)Peptide Self-Assembly to Design and Discover New Hydrogels. *Nat. Chem.* **2015**, *7*, 30–37.
- (47) Shaham-Niv, S.; Adler-Abramovich, L.; Schnaider, L.; Gazit, E. Extension of the Generic Amyloid Hypothesis to Nonproteinaceous Metabolite Assemblies. *Sci. Adv.* **2015**, *1*, No. e1500137.
- (48) Shaham-Niv, S.; Rehak, P.; Vuković, L.; Adler-Abramovich, L.; Král, P.; Gazit, E. Formation of Apoptosis-Inducing Amyloid Fibrils by Tryptophan. *Isr. J. Chem.* **2017**, *57*, 729–737.
- (49) Banik, D.; Kundu, S.; Banerjee, P.; Dutta, R.; Sarkar, N. Investigation of Fibril Forming Mechanisms of L-Phenylalanine and

L-Tyrosine: Microscopic Insight toward Phenylketonuria and Tyrosinemia Type II. *J. Phys. Chem. B* **2017**, *121*, 1533–1543.

(50) Do, T. D.; Kincannon, W. M.; Bowers, M. T. Phenylalanine Oligomers and Fibrils: The Mechanism of Assembly and the Importance of Tetramers and Counterions. *J. Am. Chem. Soc.* **2015**, *137*, 10080–10083.

(51) Perween, S.; Chandanshive, B.; Kotamarthi, H. C.; Khushalani, D. Single Amino Acid Based Self-Assembled Structure. *Soft Matter* **2013**, *9*, 10141–10145.

(52) Bera, S.; Mondal, S.; Rencus-Lazar, S.; Gazit, E. Organization of Amino Acids into Layered Supramolecular Secondary Structures. *Acc. Chem. Res.* **2018**, *51*, 2187–2197.

(53) Bera, S.; Mondal, S.; Tang, Y.; Jacoby, G.; Arad, E.; Guterman, T.; Jelinek, R.; Beck, R.; Wei, G.; Gazit, E. Deciphering the Rules for Amino Acid Co-Assembly Based on Interlayer Distances. *ACS Nano* **2019**, *132*, 1703–1712.

(54) De Luigi, A.; Mariani, A.; De Paola, M.; Re Depaolini, A.; Colombo, L.; Russo, L.; Rondelli, V.; Brocca, P.; Adler-Abramovich, L.; Gazit, E.; Del Favero, E.; Cantù, L.; Salmona, M. Doxycycline Hinders Phenylalanine Fibril Assemblies Revealing Apotential Novel Therapeutic Approach in Phenylketonuria. *Sci. Rep.* **2015**, *5*, 15902.

(55) Ihlefeldt, F. S.; Pettersen, F. B.; von Bonin, A.; Zawadzka, M.; Görbitz, C. H. The Polymorphs of L-Phenylalanine. *Angew. Chem., Int. Ed.* **2014**, *53*, 13600–13604.

(56) Knowles, T. P. J.; Mezzenga, R. Amyloid Fibrils as Building Blocks for Natural and Artificial Functional Materials. *Adv. Mater.* **2016**, *28*, 6546–6561.

(57) Do, T. D.; De Almeida, N. E. C.; LaPointe, N. E.; Chamas, A.; Feinstein, S. C.; Bowers, M. T. Amino Acid Metaclusters: Implications of Growth Trends on Peptide Self-Assembly and Structure. *Anal. Chem.* **2016**, *88*, 868–876.

(58) Amdursky, N.; Stevens, M. M. Circular Dichroism of Amino Acids: Following the Structural Formation of Phenylalanine. *ChemPhysChem* **2015**, *16*, 2768–2774.

(59) Lee, C.; Wei, X. D.; Kysar, J. W.; Hone, J. Measurement of the Elastic Properties and Intrinsic Strength of Monolayer Graphene. *Science* **2008**, *321*, 385–388.

(60) Bera, S.; Mondal, S.; Xue, B.; Shimon, L. J. W.; Cao, Y.; Gazit, E. Rigid Helical-Like Assemblies from a Self-Aggregating Tripeptide. *Nat. Mater.* **2019**, *18*, 503–509.

(61) Kol, N.; Adler-Abramovich, L.; Barlam, D.; Shneck, R. Z.; Gazit, E.; Rouso, I. Self-Assembled Peptide Nanotubes are Uniquely Rigid Bioinspired Supramolecular Structures. *Nano Lett.* **2005**, *5*, 1343–1346.

(62) Smith, S. B.; Cui, Y.; Bustamante, C. Overstretching B-DNA: The Elastic Response of Individual Double-Stranded and Single-Stranded DNA Molecules. *Science* **1996**, *271*, 795–799.

(63) Singh, R. P.; Blossey, R.; Cleri, F. Structure and Mechanical Characterization of DNA I-Motif Nanowires by Molecular Dynamics Simulation. *Biophys. J.* **2013**, *105*, 2820–2831.

(64) Smith, J. F.; Knowles, T. P. J.; Dobson, C. M.; MacPhee, C. E.; Welland, M. E. Characterization of the Nanoscale Properties of Individual Amyloid Fibrils. *Proc. Natl. Acad. Sci. U. S. A.* **2006**, *103*, 15806–15811.

(65) Uyaver, S.; Hernandez, H. W.; Habiboglu, M. G. Self-Assembly of Aromatic Amino Acids: A Molecular Dynamics Study. *Phys. Chem. Chem. Phys.* **2018**, *20*, 30525–30536.

(66) Gasymov, O. K.; Glasgow, B. J. ANS Fluorescence: Potential to Augment the Identification of the External Binding Sites of Proteins. *Biochim. Biophys. Acta, Proteins Proteomics* **2007**, *1774*, 403–411.

(67) Sirangelo, I.; Malmö, C.; Casillo, M.; Irace, G. Resolution of Tryptophan–ANS Fluorescence Energy Transfer in Apomyoglobin by Site-Directed Mutagenesis. *Photochem. Photobiol.* **2002**, *76*, 381–384.

(68) Chaudhuri, A.; Haldar, S.; Sun, H.; Koeppe, R. E.; Chattopadhyay, A. Importance of Indole N-H Hydrogen Bonding in the Organization and Dynamics of Gramicidin Channels. *Biochim. Biophys. Acta, Biomembr.* **2014**, *1838*, 419–428.

(69) Fenwick, R. B.; Oyen, D.; Dyson, H. J.; Wright, P. E. Slow Dynamics of Tryptophan–Water Networks in Proteins. *J. Am. Chem. Soc.* **2018**, *140*, 675–682.

(70) Görbitz, C. H.; Törnroos, K. W.; Day, G. M. Single-Crystal Investigation of L-Tryptophan with $Z=16$. *Acta Crystallogr., Sect. B: Struct. Sci.* **2012**, *B68*, 549–557.

(71) Li, Y.; Beck, R.; Huang, T.; Choi, M. C.; Divinagracia, M. Scatterless Hybrid Metal–Single-Crystal Slit for Small Angle X-Ray Scattering and High-Resolution X-Ray Diffraction. *J. Appl. Crystallogr.* **2008**, *41*, 1134–1139.

(72) Sheldrick, G. M. *SHELXL-2013*, Program for Crystal Structure Refinement; University of Göttingen: Göttingen, Germany, 2013.

(73) Phillips, J. C.; Braun, R.; Wang, W.; Tajkhorshid, E.; Villa, E.; Chipot, C.; Skeel, R. D.; Kale, L.; Schulten, K. Scalable Molecular Dynamics with NAMD. *J. Comput. Chem.* **2005**, *26*, 1781–1802.

(74) MacKerell, A. D.; Bashford, D. All-Atom Empirical Potential for Molecular Modeling and Dynamics Studies of Proteins. *J. Phys. Chem. B* **1998**, *102*, 3586–3616.

(75) Darden, T.; York, D.; Pedersen, L. Particle Mes Ewald: An N log(N) Method for Ewald Sums in Large Systems. *J. Chem. Phys.* **1993**, *98*, 10089–10092.

(76) Humphry, W.; Dalke, A.; Schulten, K. VMD – Visual Molecular Dynamics. *J. Mol. Graphics* **1996**, *14* (1), 33–38.